Title

Bacterial selenocysteine synthase structure revealed by single-particle cryoEM

Authors

Serrão, Vitor Hugo Balasco

Minari, Karine

Pereira, Humberto D'Muniz

et al.

Publication Date

2024

DOI

10.1016/j.crstbi.2024.100143

Peer reviewed

Current Research in Structural Biology 7 (2024) 100143

Contents lists available at ScienceDirect

Current Research in Structural Biology

journal homepage: www.journals.elsevier.com/current-research-in-structural-biology

Short Communication

Bacterial selenocysteine synthase structure revealed by single-particle cryoEM

Vitor Hugo Balasco Serrão [a,b,*], Karine Minari [c], Humberto D'Muniz Pereira [d], Otavio Henrique Thiemann [d,**]

[a] Biomolecular Cryoelectron Microscopy Facility, University of California - Santa Cruz, Santa Cruz, CA, 95064, United States
[b] Department of Chemistry and Biochemistry, University of California - Santa Cruz, Santa Cruz, CA, 95064, United States
[c] Biomolecular Engineering Department, Jack Baskin School of Engineering, University of California - Santa Cruz, Santa Cruz, CA, 95064, United States
[d] Physics Institute of Sao Carlos, University of Sao Paulo, Trabalhador Sao Carlense Av., 400, São Carlos, SP, CEP 13566-590, Brazil

ARTICLE INFO

Handling Editor: Dr. N Strynadka

Keywords:
Selenocysteine
Selenocysteine synthase
SelA
tRNA[Ser]Sec
Single-particle analysis

ABSTRACT

The 21st amino acid, selenocysteine (Sec), is synthesized on its dedicated transfer RNA (tRNA^{Sec}). In bacteria, Sec is synthesized from Ser-tRNA$^{[Ser]Sec}$ by Selenocysteine Synthase (SelA), which is a pivotal enzyme in the biosynthesis of Sec. The structural characterization of bacterial SelA is of paramount importance to decipher its catalytic mechanism and its role in the regulation of the Sec-synthesis pathway. Here, we present a comprehensive single-particle cryo-electron microscopy (SPA cryoEM) structure of the bacterial SelA with an overall resolution of 2.69 Å. Using recombinant *Escherichia coli* SelA, we purified and prepared samples for single-particle cryoEM. The structural insights from SelA, combined with previous *in vivo* and *in vitro* knowledge, underscore the indispensable role of decamerization in SelA's function. Moreover, our structural analysis corroborates previous results that show that SelA adopts a pentamer of dimers configuration, and the active site architecture, substrate binding pocket, and key K295 catalytic residue are identified and described in detail. The differences in protein architecture and substrate coordination between the bacterial enzyme and its counterparts offer compelling structural evidence supporting the independent molecular evolution of the bacterial and archaea/eukarya Ser-Sec biosynthesis present in the natural world.

1. Introduction

The crucial micronutrient selenium is essential for the well-being of animals (Rayman, 2000; Stadtman, 1974). Selenium assumes a critical role within proteins such as its incorporation into the 21st proteinogenic amino acid, referred to as selenocysteine (Sec). In selenocysteine, the sulfur group of cysteine is substituted by a selenol group (Cone et al., 1976; Serrão and Scortecci, 2020; Stadtman, 1996). Sec plays a crucial role in various redox enzymes, and it is encoded by a UGA stop codon, found in all three domains of life (Gonzalez-Flores et al., 2013). Notably, Sec does not possess its own aminoacyl-tRNA synthetase and is instead synthesized through a tRNA-dependent conversion of serine (de Freitas Fernandes et al., 2020; Gonzalez-Flores et al., 2013; Serrão et al., 2018). The initial step in Sec synthesis involves the formation of Ser-tRNA^{Sec} by seryl-tRNA synthetase (SerRS), yielding an intermediate L-seryl-(Ser)-tRNA$^{[Ser]Sec}$. Typically, aminoacyl-tRNA synthetases are highly specific enzymes that recognize and charge tRNA molecules with their corresponding amino acids. However, SerRS, a class II aminoacyl-tRNA synthetase, exhibits a unique recognition pattern for the acceptor arm and the long variable arm, of both Ser and Sec tRNAs, which results in a lack of specificity towards the anticodon (Böck and Thanbichler, 2004; Schimmel and Söll, 1979; Serrão et al., 2018).

The conversion from L-seryl-(Ser)-tRNA$^{[Ser]Sec}$ to L-selenocysteyl-tRNA^{Sec} varies across different domains of life (Böck et al., 1991a, 1991b; Forchhammer and Böck, 1991a; Manzine et al., 2013b; Serrão et al., 2018). In bacteria, Ser-tRNA$^{[Ser]Sec}$ is delivered to a homo-decameric enzyme classified as a fold-type-I pyridoxal 5′-phosphate (PLP)-dependent enzyme (Eliot and Kirsch, 2004; Itoh et al., 2013), named Selenocysteine Synthase (SelA, E.C. 2.9.1.1), or phosphoseryl-tRNA kinase - PSTK - in Archaea/Eukarya) for the conversion of Ser to Sec (Engelhardt et al., 1992; Forchhammer and Böck, 1991b; Itoh et al., 2013; Manzine et al., 2013a, 2013b). This enzyme was

* Corresponding author. Biomolecular Cryoelectron Microscopy Facility, University of California - Santa Cruz, Santa Cruz, CA, 95064, United States.
** Corresponding author.
E-mail addresses: vbalasco@ucsc.edu (V.H. Balasco Serrão), thiemann@ifsc.usp.br (O.H. Thiemann).

https://doi.org/10.1016/j.crstbi.2024.100143
Received 20 November 2023; Received in revised form 31 March 2024; Accepted 9 April 2024
Available online 16 April 2024

Table 1
CryoEM data collection, single-particle reconstruction maps, and model statistics.

Data collection information	*PNCC #160058 – Krios-3*
Nominal magnification	105,000x
Voltage (kV)	300
Electron dose (e^{-}/Å^2)	45.4
Physical pixel size (super-res) (Å)	0.826 (0.413)
Movies amount	4592
Defocus average and range (μm)	1.7 (0.6–2.8)
Frames	60
Single-particle reconstruction information	**EMDB-42845**
Initial particles picked	868,381
Particles in the final map	223,410
Initial model used	Ab initio
Symmetry imposed	D5
Map overall resolution - $FSC_{0.143}$ (Å)	2.69
Map resolution range (Å)	2.2 to 6.0
Map sharpening B-factor (Å^2)	93.5
Built model information	**PDB 8UZW**
Chains	10
Atoms (non-H)	28,258 (H: 0)
Protein residues	3713
Ligands	240 (H:0)
Bonds (RMSD)	
Length (Å, # > 4σ)	0.011 (12)
Angles (°,# > 4σ)	1.154 (35)
Mean B-factor (Å^2)	28258/0
Protein (min/max/mean)	0.00/183.56/88.13
MolProbity score	1.63
Clashscore	9.14
Rotamers outliers (%)	0.67
Ramachandran plot	
Favored (%)	97.24
Allowed (%)	2.76
Favored (%)	0
Rama-Z (Ramachandran plot Z-score, RMSD)	
Whole (N = 3625)	0.78 (0.14)
Helix (N = 1443)	1.18 (0.14)
Sheet (N = 472)	0.31 (0.23)
Loop (N = 1710)	0.14 (0.16)
Rotamer outliers (%)	0.71
Cβ outliers (%)	0.00
Peptide plane (%)	
Cis proline/general	0.0/0.0
Twisted proline/general	0.0/0.0
CaBLAM outliers (%)	1.83
Occupancy	
Mean	1.00
occ = 1 (%)	100.00
0 < occ <1 (%)	0.00
occ >1 (%)	0.00
Model vs. Data	
Mean CC for ligands	–
CC (peaks)	0.61
CC (volume)	0.80
CC (box)	0.65
CC (mask)	0.81

Molecular interfaces

Monomer 1	Monomer 2	Area (Å^2)	ΔG (kcal.mol^{-1})
A	B	2797	−23.7
B	C	1058	−4.5
C	D	3010	−25.4
D	E	1077	−4.4
E	F	2883	−26.3
F	G	1061	−4.4
G	H	2960	−26.6
H	I	1050	−3.8
I	J	2924	−25.8
J	A	1050	−4.3

initially identified in *E. coli* in the 1990s (Engelhardt et al., 1992; Forchhammer and Böck, 1991b), where it was found to convert Ser to Sec in a two-step process. In the first step, a *Schiff's* base is formed between the α-amino group of L-serine and the formyl group of a covalently bound PLP located in the catalytic lysine residue of SelA. This reaction leads to the dehydration of Ser and the formation of an intermediate state known as aminoacrylyl-tRNA^{Sec}, which becomes covalently linked to SelA in the acceptor arm (de Freitas Fernandes et al., 2020; Forchhammer and Böck, 1991b). The second step involves selenium transfer through nucleophilic substitution, resulting in the creation of Sec-tRNA^{Sec}. The biologically active selenium in the form of monoselenophosphate (H_2SePO^{3-}) is supplied by selenophosphate synthetase (SelD in *Bacteria* or SPS in Eukarya, E.C. 2.7.9.3) (Noinaj et al., 2012; Silva et al., 2015). A 1.3 MDa transient complex assembles through the interaction of SelA. Ser-tRNA$^{[Ser]Sec}$ and SelD, which delivers the selenium, as monoselenophosphate, and provides the catalytic pocket for the production of mature Sec-tRNA^{Sec} (Serrão et al., 2018; Silva et al., 2015).

In 2013, Manzine et al. (2013b) determined that the stoichiometric ratio between *E. coli* SelA decamers and tRNA^{Sec} as 1:10, consistent with the crystal structure of *Thermocatellispora tengcongensis* tRNA^{Sec}–*Aquifex aeolicus* SelA, which shares only 30% amino acid sequence identity with *E. coli* SelA (Itoh et al., 2013). Itoh and collaborators demonstrated that the N-terminal three-helix bundle of each *A. aeolicus* SelA monomer in the homo-decamer has a strong affinity for the D-arm region and the TΨC loop of tRNA^{Sec}, with no interactions observed with either the extra arm or the anticodon arm (Itoh et al., 2013). The D-arm region of tRNA^{Sec} was identified as the primary recognition determinant for SelA in Ser–tRNA^{Sec}, distinguishing it from Ser–tRNA^{Ser}. These crystallographic structures at 3.9 Å (*Aa*SelA) and 7.5 Å (*Aa*SelA-tRNA^{Sec}) were the first tridimensional structural evidence in a subnanometric resolution to describe the complex formation and function.

It is imperative for all Sec-synthesis systems to accurately discriminate between Ser-tRNA^{Sec} and Ser-tRNA^{Ser}. tRNA^{Sec} is notably the longest tRNA (Schön et al., 1989; Serrão et al., 2018), and its tertiary structure differs significantly from that of a typical tRNA (Itoh et al., 2009; Palioura et al., 2009). In Archaea and Eukarya, PSTK functions to discern between Ser-tRNA$^{[Ser]Sec}$ and Ser-tRNA^{Ser} for the phosphorylation process (Chiba et al., 2010; Serrão et al., 2018). Following this, SepSecS identifies Sep-tRNA$^{[Ser]Sec}$ in a phosphate-dependent manner (Palioura et al., 2009).

Initial cryogenic electron microscopy has suggested that SelA is a homo-decameric enzyme with a molecular weight exceeding 500 kDa (Engelhardt et al., 1992; Fischer et al., 2007; Manzine et al., 2013b; Serrão et al., 2014), however, the lack of SelA high-resolution structural data has left the discrimination mechanism in bacteria unclear. In this study, we present high-resolution single-particle cryoEM reconstruction of full-length decameric *Escherichia coli* SelA covalently-bound to PLP (SelA, full-length construct defined from residue 1 to 463) at an overall gold-standard resolution ($FSC_{0.143}$) of 2.69 Å and local resolution varying between 2.2 and 6.0 Å. Additionally, profound structural analysis in high-resolution details corroborates the previous crystallographic and low-resolution cryoEM data.

2. Materials and methods

2.1. Selenocysteine synthetase expression and purification

E. coli Selenocysteine Synthase (SelA) has been extensively studied and its expression and purification protocol were previously established by Manzine et al. (Manzine et al., 2013a, 2013b). The *selA* gene (UniProt #P0A821) was inserted in pET29a (+) vector and transformed into a modified *E. coli* WL81640 (λ-DE3). Cells were grown for 3 h until O. $D._{600nm}$ 1.0 followed by the addition of 0.1 mM IPTG. After cell lysis by sonication, the protein extract was submitted to salting-out precipitation in 25% w/v ammonium sulfate, then the sediment was suspended and desalted on a 5 mL-HiTrap Desalting column (GE) followed by size

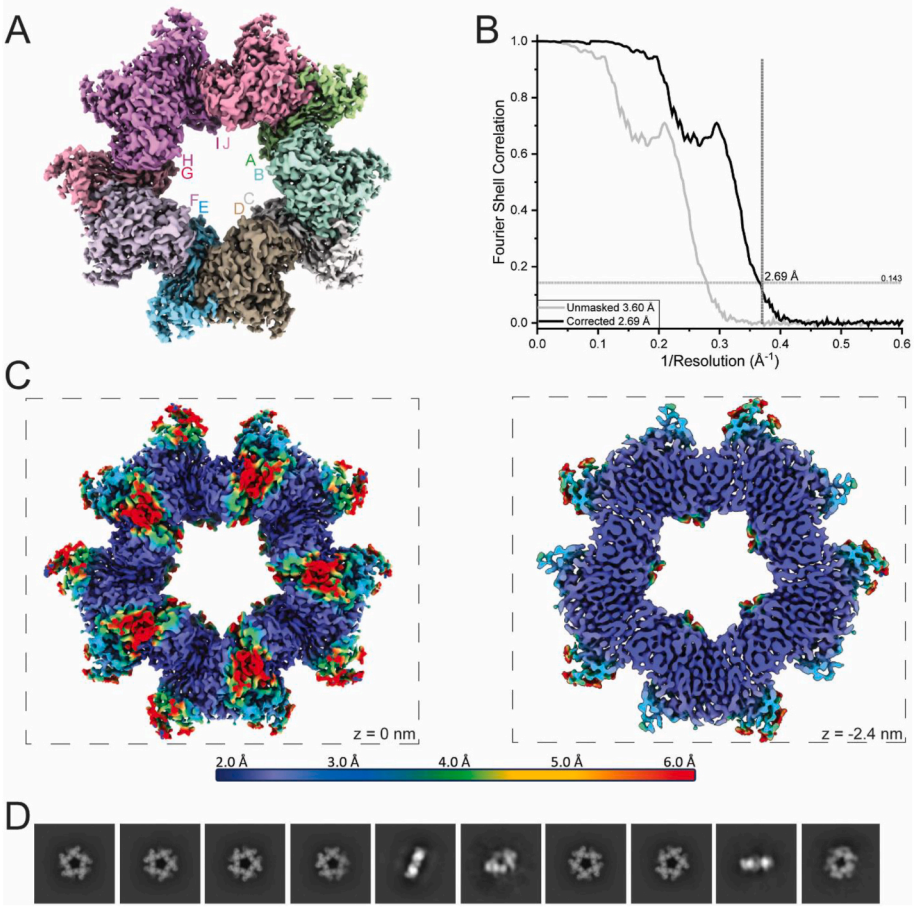

Fig. 1. Bacterial SelA single-particle cryoEM reconstruction. (A) Single particle cryoEM 3D reconstructed map using D5 symmetry colored by chain (A–J). (B) $FSC_{0.143}$ overall resolution estimation resulted at 2.69 Å. (C) Local resolution estimation (2.2–6.0 Å) heat map from the entire molecule and the cross-section at z = −24 Å, related to half of the map depth. The dashed boxes represent the z plane in each section (D) 2D classes are used for map reconstruction and structure determination.

exclusion chromatography using GE Superdex 200 16/60 in buffer 20 mM potassium phosphate pH 7.5, 100 mM sodium chloride, 2 mM β-mercaptoethanol, and 10 μM pyridoxal 5′-phosphate (PLP). The recombinant SelA fractions were collected and concentrated by ultrafiltration using a cellulose matrix 30 kDa-cutoff filter (Amicon). Final concentration estimation was obtained spectrophotometrically at 280 nm by considering the predicted aromatic amino acids content and the predicted molar extinction coefficient (ε = 35410 $M^{-1}cm^{-1}$).

2.2. Single-particle cryoEM sample preparation and data collection

Purified SelA was concentrated to 77 μM at 4 °C and a 3.5 μl aliquot was deposited onto Quantfoil R 1.2/1.3400 mesh grid (EM Sciences) after undergoing a glow discharge with an Easy Pelco Glow-discharger. Any excess sample was blotted for 2.5 s using a force of −10 and 100% humidity at 22 °C and then swiftly plunged frozen into liquid ethane using the Vitrobot Mark IV (Thermo Fisher) located at the Biomolecular cryoEM facility at UCSC Biomolecular cryoEM facility. The frozen grids were screened in a Glacios microscope (Thermo Fisher) operating at 200 kV and equipped with a Gatan K2 Summit direct detector. Top-selected grids were used for data collection at the Pacific Northwest CryoEM center (PNCC proposal 160058 – Oregon/US).

Data collection was performed on a Titan Krios G3i at 300 kV equipped with a Gatan K3 direct detector coupled to a Bioquantum energy filter at 105,000X at a super-resolution counting mode with a physical pixel size of 0.826 Å/pix (super-res 0.413 Å/pix). A total of 4592 movies were collected in a stack of 60 frames, and a total dose of 45.4 $e^{-}/Å^{2}$.

2.3. Single-particle cryoEM data processing

The 4592 movies were preprocessed using cryoSPARC v4.2.1 (Punjani et al., 2017) by patch motion correction and CTF correction. After movie curation (3821 selected movies), 1281 particles were manually picked for generating templates for the automated particle picking. After two rounds of template picking, the particles were further selected through 2D classification, resulting in 688,602 particles used at the initial 3D classification. Particles belonging to the representative group were submitted to another 2D classification round for further cleaning and submitted to non-uniform refinement followed by homogeneous refinement using D5 symmetry. A final cycle of local-CTF refinement and local refinement was conducted in order to improve the map quality with the automatically generated mask in the previous steps, using the file 223,410 top-selected particles. A final "gold standard" resolution of 2.69 Å was achieved for the reconstructed map and a local resolution range between 2.2 and 6.0 Å.

2.4. Model building and structural analysis

The initial model for *E. coli* SelA was generated by AlphaFold2 (Jumper et al., 2021) and docked into the map using Coot v0.9.4 (Emsley and Cowtan, 2004). Further modeling, coordinate refinement, and energy minimization were performed using Coot v0.9.4 and Phenix v. 1.20.1-4487 (Afonine et al., 2012; Liebschner et al., 2019). The

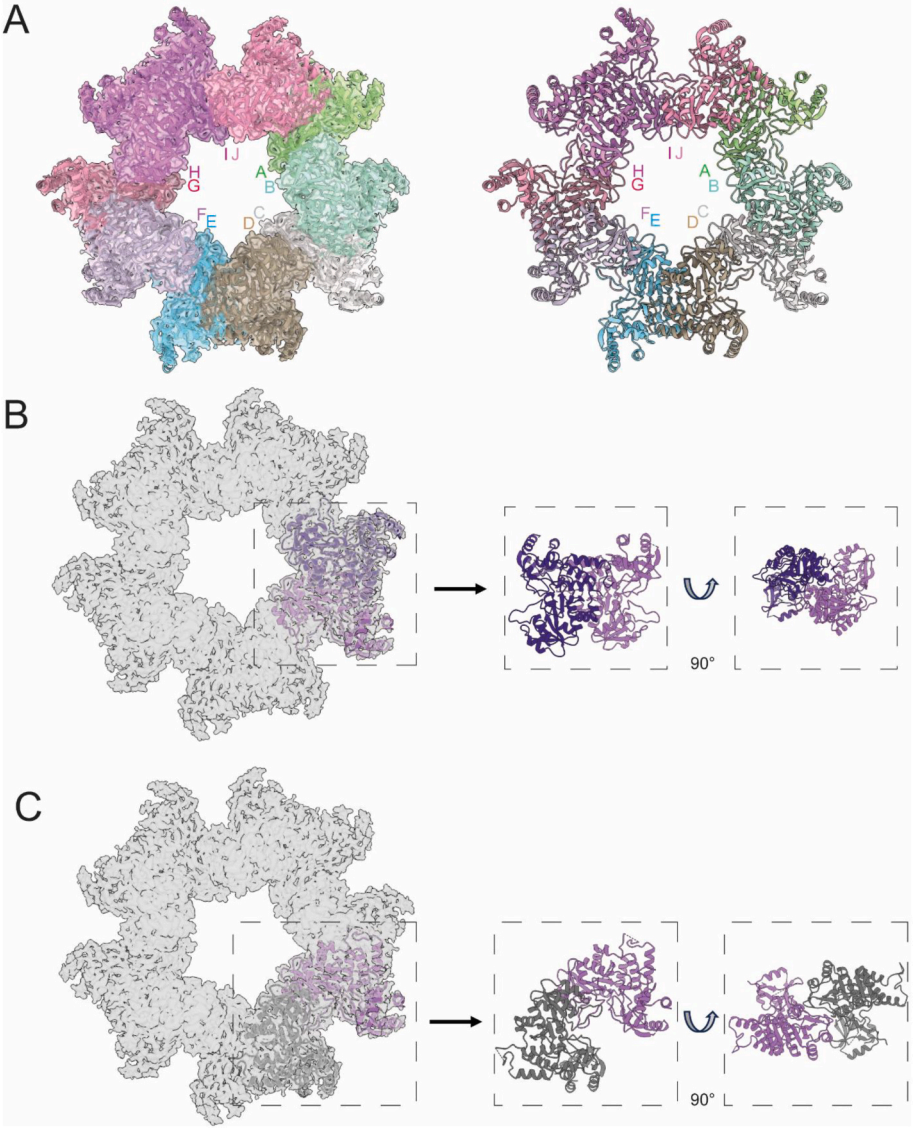

Fig. 2. Model built and structure analysis. (A) Map-to-model fit and structure details showing SelA homo-decameric conformation (A–J). (B) Canonical fold-type-I PLP-dependent enzymes and dimeric interaction. (C) Dimeric conformation is responsible for the Ser-tRNA$^{[Ser]Sec}$ binding pocket, This unique orientation results in a considerable gap between the core and C-terminal domains, facilitating interaction with the neighboring intimate dimer for the formation of the decamer and the creation of a substantial cleft between two dimers.

flexible N-terminal (1–76) and flexible loop (122–127) were not observed in the reconstructed map. Validation was performed using FSC-Q (Ramírez-Aportela et al., 2021) and model-to-map criteria (Afonine et al., 2018). The electrostatic potential calculation was performed using eF-surf (PDBj) server (Kinoshita and Nakamura, 2004). The molecular interfaces were analyzed using PDBePISA (Paxman and Heras, 2017) and represented in Table 1.

The maps and model were deposited in the Electron Microscopy Databank and Protein Data Bank, respectively, with accession numbers EMDB-42845 and PDB.ID 8UZW. Data collection and model refinement parameters are reported in Table 1. Figures were generated using UCSF Chimera-X (Meng et al., 2023) and PyMOL Molecular Graphics System (version 1.7 Schrodinger, LLC).

3. Results and discussion

3.1. CryoEM reconstruction of bacterial SelA

Low-resolution structures of bacterial SelA have been solved using single-particle analysis from negative stain (NS-TEM) or cryogenic samples (cryoEM) (Engelhardt et al., 1992; Fischer et al., 2007; Manzine et al., 2013b; Serrão et al., 2014). The low-resolution of negative staining techniques limited our ability to directly visualize the stoichiometry and connectivity of the subunits, as well as their interaction with the tRNA^{Sec} for the analyzed complexes (Engelhardt et al., 1992; Serrão et al., 2014). Only using principal components analysis (PCA-EM) from negatively stained data, Manzine et al. were able to unequivocally define the SelA.tRNA$^{[Ser]Sec}$ stoichiometry (Manzine et al., 2013b). Crystal structures provided snapshots of SelA macromolecular assembly and its complex with tRNA^{Sec} (Itoh et al., 2013), however, we used cryoEM methods to elucidate the fine detail of this macromolecular machinery and gain a deeper understanding of its molecular structure at a high-resolution (Table 1).

We obtained a 3D-reconstruction *E. coli* SelA map (Fig. 1A) and consequently a model containing 10 protomers associated as a unique D5-symmetry decamer at a final overall resolution of 2.69 Å (Fig. 1B). The analysis of the local resolution of the map (Fig. 1C), showing local resolutions in the range 2.2–6.0 Å, suggested that SelA presented an

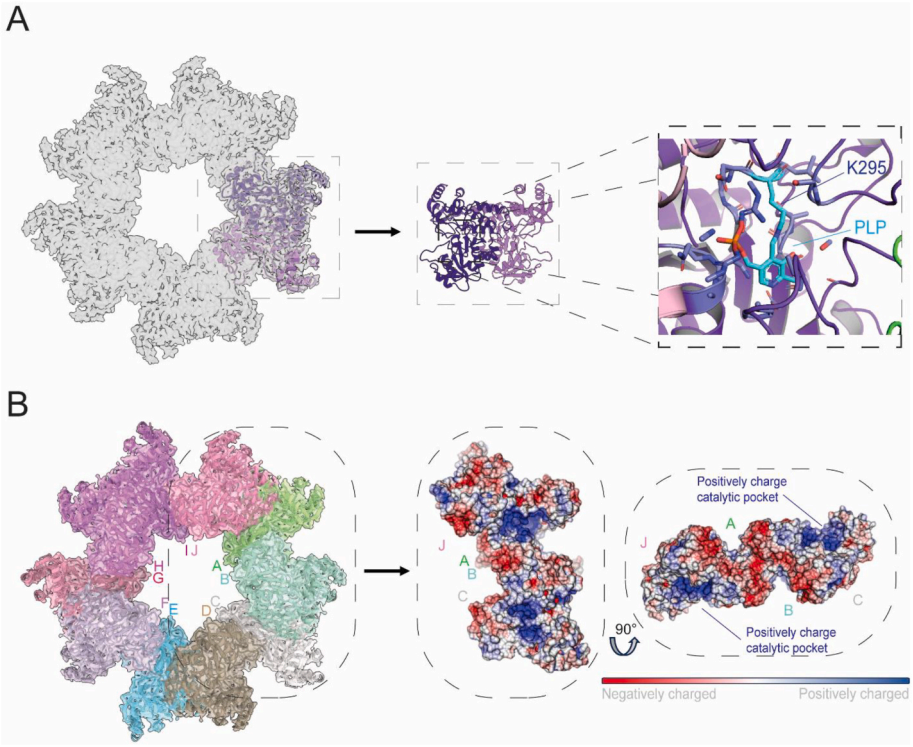

Fig. 3. Structure highlights. (A) Canonical SelA dimer showing the K295-covalently bound PLP active site. (B) The electrostatic potential surface of two consecutive dimers highlights the positively charged Ser-tRNA$^{[Ser]Sec}$ binding pocket between dimers.

inherent flexibility, particularly with respect to the movement of the N-terminal domain.

SelA 2D-classes clearly presented D5 symmetry (Fig. 1D), previously elucidated by several reports (Engelhardt et al., 1992; Manzine et al., 2013b; Serrão et al., 2014), we, therefore, imposed a D5 symmetry in the homogeneous and local refinements cycles in order to improve the quality of the map and also the overall resolution.

3.2. Structure determination and analysis

Bacterial SelA is a homo-decamer, where the ten subunits assemble into a pentamer-of-dimers configuration (Fig. 2A) similar to previous observations from the crystal structure of *A. aeolicus* SelA (Itoh et al., 2013). Each subunit comprises four distinct segments; the N-terminal domain (residues 1 to 66, not observed in the reconstructed map probably due to flexibility in solution), the N-linker (residues 67 to 89), the core domain (residues 90 to 338), and the C-terminal domain (residues 339 to 463). Hence, the quaternary structure of a pentamer of dimers is pivotal for SelA's function. The pentamer of dimers formed by subunits A/B; C/D; E/F; G/H and I/J presented extensive buried area, in agreement with previous observations from Itoh and collaborators (Itoh et al., 2014). SelA decamer is exclusively observed in bacteria (Itoh et al., 2012, 2013; Silva et al., 2015).

Within the SelA dimer, two catalytic sites are established at the interface between the subunits (Fig. 2B). These sites involve the covalent attachment of the cofactor pyridoxal 5′-phosphate (PLP) to a conserved K295 residue (Fig. 3A). Moreover, there is a significant positively charged crevice between two SelA dimers (Fig. 3B) that accommodates the 3′-terminal region of Ser–tRNA^{Sec}, including the acceptor stem and the G73 discriminator, although it was not entirely visible in the crystal structure (Itoh et al., 2013).

Furthermore, the N-terminal domain is crucial for SelA oligomerization (Itoh et al., 2013; Silva et al., 2015). In the previous crystal structure (Itoh et al., 2013), the N-terminal domain extends outward from the central pentagon, displaying intrinsic flexibility, which agreed with our 3D reconstruction and limited its visualization using single-particle cryoEM. Apart from its role in decamer formation, the N-terminal domain of SelA also contributes to tRNA^{Sec} recognition, while the SelA dimeric sub-structure is essential for constructing a functional active site between the dimer interfaces (Itoh et al., 2013, 2014; Kaiser et al., 2005). Interestingly, the genome of the Archaea *Methanocaldococcus jannaschii* contains a putative SelA gene that lacks an N-terminal domain (Kaiser et al., 2005). Structural studies have revealed that this form of SelA assembles as a dimeric structure without known biological activity and does not interact with tRNA^{Sec} (Fig. 2A and B) (Itoh et al., 2014; Kaiser et al., 2005; Silva et al., 2015).

On the other hand, the well-resolved C-terminal domain revealed that its orientation, concerning the core domain, significantly deviates from the arrangement observed in other fold-type-I PLP-dependent enzymes (Eliot and Kirsch, 2004). This unique orientation results in a considerable gap between the core and C-terminal domains, facilitating interaction with the neighboring dimer forming the decamer and creating a substantial cleft between two dimers (Figs. 2B and 3B). Comparatively, *E. coli* SelA presents a canonical fold-type-I PLP-dependent as putative archaeal selenocysteine synthase (PDB ID 2AEU) (Kaiser et al., 2005) and the depentamerized mutant of N-terminal truncated selenocysteine synthase SelA from *A. aeolicus* (PDB ID 3WCO and 3WCN) (Itoh et al., 2014). Moreover, the structural comparison shows that *E. coli* SelA presented similar folding as observed for dimeric putative archaeal SelA from *M. jannaschii* (PDB.ID 2AEU) and *A. aeolicus* dimeric SelA from Y220P-D199R-T191Y-T192Y mutant (PDB.ID 3WCN) and N-terminal (1–61) truncation (SelA-ΔN, PDB.ID 3WCO) (Fig. 4).

SelA's dimeric core conformation was proposed as a "SelA ancestor" (Itoh et al., 2014) and may have been an enzyme involved in sulfur metabolism. The ancestral dimeric SelA engaged the tRNA^{Sec} acceptor arm in the cleft between the core and C-terminal domains, relying on the Sep-phosphate group at the monoselenophosphate binding site for interaction with Sep-tRNA^{Sec}, making the Sep-to-Sec reaction and tRNA discrimination contingent on the Sep-phosphate group. Moreover, the PLP-pocket comparison in the close state from *E. coli* SelA with

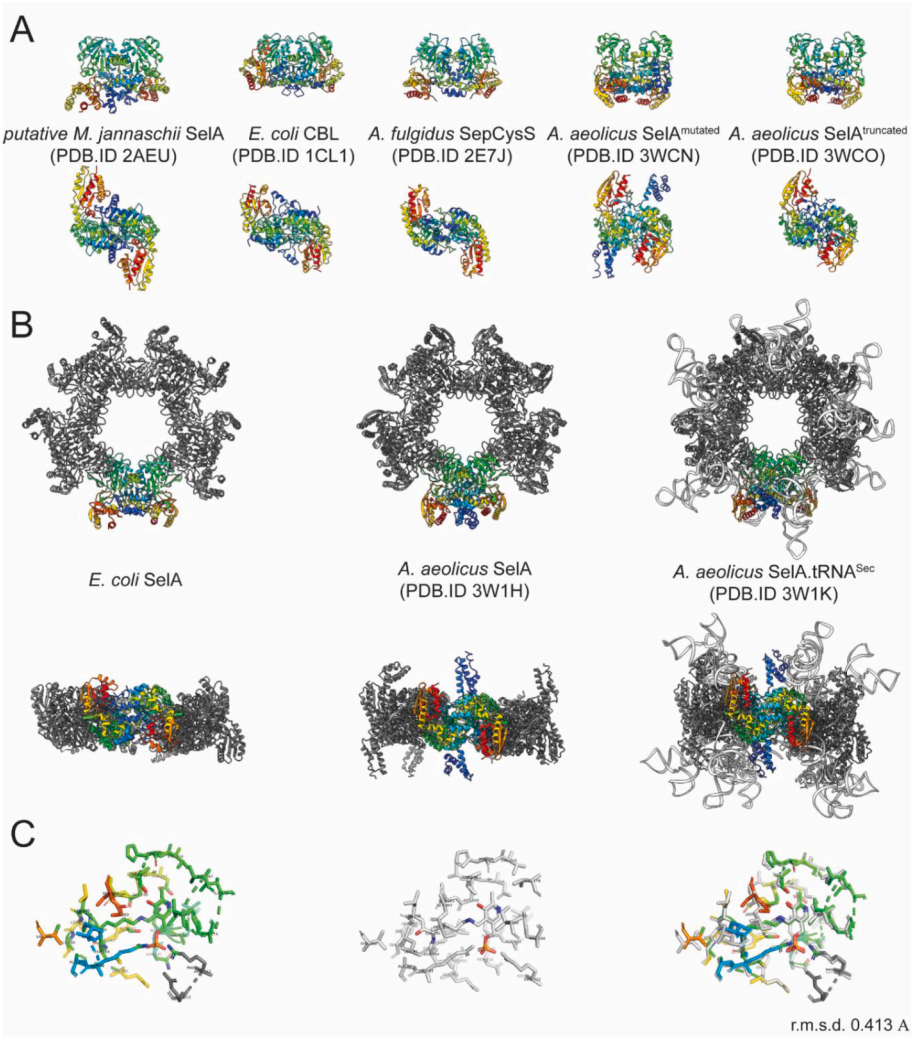

Fig. 4. Fold-type-I PLP-dependent canonical folding. (A) Overall fold-type-I PLP-dependent structural comparison of dimeric putative archaeal SelA from *M. jannaschii* (PDB.ID 2AEU), bacterial cystathionine β-lyase (CBL, PDB.ID 1CL1), archaeal Sep-tRNA:Cys-tRNA synthase (SepCysS, PDB.ID 2E7J) and *A. aeolicus* dimeric SelA from Y220P-D199R-T191Y-T192Y mutant (PDB.ID 3WCN) and N-terminal (1–61) truncation (SelA-ΔN, PDB.ID 3WCO). (B) Decameric SelAs from *E. coli*, *A. aeolicus* (PDB.ID 3W1H), and SelA.tRNA^{Sec} complex (PDB.ID 3W1K). (C) From left to right, PLP-pocket comparison in close state from *E. coli* SelA with *A. aeolicus* SelA and the superposition showing the highly conserved sequence and r.m.s.d. of 0.413 Å. PDB.IDs are represented in the figure and the molecules are colored in a rainbow from N-(blue) to C-(red) terminal. (For interpretation of the references to color in this figure legend, the reader is referred to the Web version of this article.)

A. aeolicus SelA and the superposition showing the highly conserved sequence and r.m.s.d. of 0.413 Å and similar to *A. aeolicus* SelA.tRNA^{Sec}, also found in a closed state and 23 Å distant from the 3′-CCA-tRNA^{Sec} (Fig. 4C).

Interestingly, bacterial SelA catalyzes the Sec formation using a distinct set of K295-PLP bound active-site, distinct from the Arg residues present in the *Archaea* and *Eukarya* paralogue SepSecS (Palioura et al., 2009). *E. coli* SelA's unique C-terminal domain orientation positions the N-terminal specifically, allowing its participation in the catalytic site and facilitating the interaction between Arg97 and Lys295. The distinctive tertiary and quaternary structures of SelA are essential for its specialized catalytic activity in hydroxyl group elimination. Comparatively, human SepSecS-Arg75, occupies a space corresponding to SelA's Arg97, however, in the core domain. Notably, Arg75 in SepSecS engages in inter-subunit interaction with Lys-bound PLP, whereas SelA's Arg97 interacts intra-subunitly with PLP-Lys295. Furthermore, SepSecS, due to the inability of PLP-Lys284, cannot protonate the β-hydroxyl group of the Ser moiety, preventing it from binding Ser-tRNA^{Sec}, as the phosphate group is crucial for substrate Sep-tRNA^{Sec} binding.

Itoh and collaborators suggested that tetramerization allows the formation of an A76-binding pocket in *A. aeolicus* SelA, and decamerization enhances stability among close dimers (Itoh et al., 2014). The N-terminal plays a crucial role in distinguishing tRNA$^{[Ser]Sec}$ from tRNA^{Ser} by interacting with the unique D-arm of tRNA^{Sec} (Itoh et al., 2013). This secondary-binding pocket and tRNA^{Sec} discrimination enabled Ser-to-Sec conversion, making SelA independent of the Sep phosphate group (Itoh et al., 2013; Manzine et al., 2013b; Silva et al., 2015). Conversely, the dimeric SepSecS interacted with the extra arm side of the tRNA^{Sec} acceptor arm, lacking a cleft between the core and C-terminal domains (Palioura et al., 2009). On the other hand, the tetramerization of SepSecS stabilized tRNA^{Sec} binding by interacting with its TΨC and extra arms without recognizing the unique D-arm structure, leaving SepSecS unable to become independent of the Sep-phosphate group of Sep-tRNA^{Sec} (Palioura et al., 2009).

In *E. coli* SelA, this secondary binding pocket responsible for the tRNA$^{[Ser]Sec}$-variable arm recognition is comprised between the N-terminal Q77-G88 from the first subunit (i) and E430-R449 from the subsequent (n+1) subunit, forming a positively charged binding pocket (Fig. 3B).

Furthermore, the dissimilar structures and distinctive catalytic

residues found in bacteria and archaeal/eukarya Sec synthases serve as evidence for the convergent evolution of two distinct Sec synthesis systems present in nature but do not clarify the remaining question regarding the oligomerization state and conformation for its activity.

Itoh and collaborators suggested that the evolutionary collaboration of two SelA dimers potentially resulted in the development of an A76-binding pocket at the dimer–dimer interface, enhancing substrate binding efficiency (Itoh et al., 2014). However, in a tetramer, only two of the four catalytic sites were functional, reaching a "half-of-the-sites" stage, with subsequent stabilization of dimer orientations through a decameric ring closure (Fig. 4). The dimeric mutant and N-terminal depletion SelA exhibited a non-productive catalytic site conformation similar to other fold-type I members, suggesting a more primitive state and the evolution of the catalytic site may have taken advantage of the decameric quaternary structure, with the N-terminal domain acquired for increased affinity for $tRNA^{Sec}$ and discrimination from $tRNA^{Ser}$ (Itoh et al., 2014; Silva et al., 2015).

3.3. Concluding remarks

Here, we have presented the cryoEM reconstructed map and model structure of the bacterial Selenocysteine Synthase (SelA), containing 10 subunits - pentamer-of-dimers assemblies - into a ring-like structure capable of binding ten $tRNA^{Sec}$ molecules and resulting in a molecular weight of ~0.5 MDa, at a near-atomic detail. The unique homo-decameric and highly symmetrical arrangement are unique in bacteria and its function is still not fully understood. Why do bacteria require a huge homo-decamer complex and *Archaea* and *Eukarya* do not?

Moreover, SelA N-terminal domain plays a pivotal role in recognizing the specific D-arm structure of $tRNA^{Sec}$, thereby enabling the discrimination between Ser-$tRNA^{[Ser]Sec}$ and Ser-$tRNA^{Ser}$ (Itoh et al., 2013, 2014; Kaiser et al., 2005). However, the inherent flexibility of the N-terminal domain does not allow us, at present, to obtain the entire model, which may reveal the dynamic in solution for the Ser-$tRNA^{[Ser]Sec}$ recognition and its activity during the Ser-Sec conversion, being the next target for future study. Observed the canonical fold-type-I PLP-dependent at high resolution, allowed to present the PLP interactions at a closed-state with high accuracy, corroborating with the dimeric crystal structures as well the *A. aeolicus* homo-decameric structure. The interdimer interaction and the presence of the second positively charged binding pocket are also highlighted at high-resolution even in the absence of the flexible N-terminal (1–76) region. The Ser-Sec conversion mechanism is still lacking at atomic resolution, however, this structure brings us one step closer to the full understanding of Sec biosynthesis and why it requires a large supramolecular machinery in bacteria.

Funding

We acknowledge funding from FAPESP (12/23730-1), CNPq (232251/2014-2, 140636/2013-7 and 479595/2006-2) and CAPES. A portion of this research was supported by NIH grant U24GM129547 and performed at the PNCC at OHSU and accessed through EMSL (grid.436923.9) and also the Biomolecular cryo-Electron Microscopy Facility at the Department of Chemistry and Biochemistry of the University of California - Santa Cruz (RRID:SCR_021755) for scientific and technical assistance (NIH High-End Instrumentation program, S10OD02509).

Data accessibility

The cryoEM density map has been deposited in the Electron Microscopy Data Bank under accession code EMD-42845 and coordinates have been deposited in the Protein Data Bank under the accession code PDB ID 8UZW.

CRediT authorship contribution statement

Vitor Hugo Balasco Serrão: Formal analysis, Funding acquisition, Writing – original draft. **Karine Minari:** Formal analysis, Writing – original draft. **Humberto D'Muniz Pereira:** Formal analysis, Writing – original draft. **Otavio Henrique Thiemann:** Formal analysis, Funding acquisition, Writing – original draft.

Declaration of competing interest

The authors declare that they have no known competing financial interests or personal relationships that could have appeared to influence the work reported in this paper.

Data availability

Data will be made available on request.

Acknowledgements

This work was supported by research grants from FAPESP (12/23730-1), CNPq (232251/2014-2, 140636/2013-7 and 479595/2006-2) and CAPES. We thank Dr. Omar Davulcu and the Pacific Northwest Center for CryoEM (PNCC) at Oregon Health & Science University for data collection and support on data processing. A portion of this research was supported by NIH grant U24GM129547 and performed at the PNCC at OHSU and accessed through EMSL (grid.436923.9), a DOE Office of Science User Facility sponsored by the Office of Biological and Environmental Research. We also thank Drs. Irina Novikova and Craig Yoshioka at PNCC for data processing training and support at PNCC Compute. The authors also acknowledge the Biomolecular cryo-Electron Microscopy Facility at the Department of Chemistry and Biochemistry of the University of California - Santa Cruz (RRID:SCR_021755) for scientific and technical assistance (NIH High-End Instrumentation program, S10OD02509). Molecular graphics and analyses performed with UCSF ChimeraX, developed by the Resource for Biocomputing, Visualization, and Informatics at the University of California, San Francisco, with support from National Institutes of Health R01-GM129325 and the Office of Cyber Infrastructure and Computational Biology, National Institute of Allergy and Infectious Diseases.

References

Afonine, P.V., Grosse-Kunstleve, R.W., Echols, N., Headd, J.J., Moriarty, N.W., Mustyakimov, M., Terwilliger, T.C., Urzhumtsev, A., Zwart, P.H., Adams, P.D., 2012. Towards automated crystallographic structure refinement with phenix.refine. Acta Crystallogr. D 68, 352–367. https://doi.org/10.1107/S0907444912001308.

Afonine, P.V., Klaholz, B.P., Moriarty, N.W., Poon, B.K., Sobolev, O.V., Terwilliger, T.C., Adams, P.D., Urzhumtsev, A., 2018. New tools for the analysis and validation of cryo-EM maps and atomic models. Acta Crystallogr. D 74, 814–840. https://doi.org/10.1107/S2059798318009324.

Böck, A., Forchhammer, K., Heider, J., Baron, C., 1991a. Selenoprotein synthesis: an expansion of the genetic code. Trends Biochem. Sci. 16, 463–467. https://doi.org/10.1016/0968-0004(91)90180-4.

Böck, A., Forchhammer, K., Heider, J., Leinfelder, W., Sawers, G., Veprek, B., Zinoni, F., 1991b. Selenocysteine: the 21st amino acid. Mol. Microbiol. 5, 515–520. https://doi.org/10.1111/j.1365-2958.1991.tb00722.x.

Böck, A., Thanbichler, M., 2004. Selenocysteine. EcoSal Plus 1. https://doi.org/10.1128/ecosalplus.3.6.1.1.

Chiba, S., Itoh, Y., Sekine, S., Yokoyama, S., 2010. Structural basis for the major role of O-phosphoseryl-tRNA kinase in the UGA-specific encoding of selenocysteine. Mol. Cell 39, 410–420. https://doi.org/10.1016/j.molcel.2010.07.018.

Cone, J.E., Del Río, R.M., Davis, J.N., Stadtman, T.C., 1976. Chemical characterization of the selenoprotein component of clostridial glycine reductase: identification of selenocysteine as the organoselenium moiety. Proc. Natl. Acad. Sci. U.S.A. 73, 2659–2663. https://doi.org/10.1073/pnas.73.8.2659.

de Freitas Fernandes, A., Serrão, V.H.B., Scortecci, J.F., Thiemann, O.H., 2020. Seryl-tRNA synthetase specificity for tRNAsec in bacterial sec biosynthesis. Biochim. Biophys. Acta, Proteins Proteomics 1868, 140438. https://doi.org/10.1016/j.bbapap.2020.140438.

Eliot, A.C., Kirsch, J.F., 2004. Pyridoxal phosphate enzymes: mechanistic, structural, and evolutionary considerations. Annu. Rev. Biochem. 73, 383–415. https://doi.org/10.1146/annurev.biochem.73.011303.074021.

Emsley, P., Cowtan, K., 2004. Coot: model-building tools for molecular graphics. Acta Crystallogr. D Biol. Crystallogr. 60, 2126–2132. https://doi.org/10.1107/S0907444904019158.

Engelhardt, H., Forchhammer, K., Müller, S., Goldie, K.N., Böck, A., 1992. Structure of selenocysteine synthase from Escherichia coli and location of tRNA in the seryl-tRNA (sec)-enzyme complex. Mol. Microbiol. 6, 3461–3467. https://doi.org/10.1111/j.1365-2958.1992.tb01781.x.

Fischer, N., Paleskava, A., Gromadski, K.B., Konevega, A.L., Wahl, M.C., Stark, H., Rodnina, M.V., 2007. Towards understanding selenocysteine incorporation into bacterial proteins. Biol. Chem. 388, 1061–1067. https://doi.org/10.1515/BC.2007.108.

Forchhammer, K., Böck, A., 1991a. [Biology and biochemistry of selenium]. Naturwissenschaften 78, 497–504. https://doi.org/10.1007/BF01131397.

Forchhammer, K., Böck, A., 1991b. Selenocysteine synthase from Escherichia coli. Analysis of the reaction sequence. J. Biol. Chem. 266, 6324–6328.

Gonzalez-Flores, J., Shetty, S.P., Dubey, A., Copeland, P.R., 2013. The molecular Biology of selenocysteine. Biomol. Concepts 4, 349–365. https://doi.org/10.1515/bmc-2013-0007.

Itoh, Y., Bröcker, M.J., Sekine, S., Hammond, G., Suetsugu, S., Söll, D., Yokoyama, S., 2013. Decameric SelA•tRNA(Sec) ring structure reveals mechanism of bacterial selenocysteine formation. Science 340, 75–78. https://doi.org/10.1126/science.1229521.

Itoh, Y., Bröcker, M.J., Sekine, S., Söll, D., Yokoyama, S., 2014. Dimer-dimer interaction of the bacterial selenocysteine synthase SelA promotes functional active-site formation and catalytic specificity. J. Mol. Biol. 426, 1723–1735. https://doi.org/10.1016/j.jmb.2014.01.003.

Itoh, Y., Chiba, S., Sekine, S.-I., Yokoyama, S., 2009. Crystal structure of human selenocysteine tRNA. Nucleic Acids Res. 37, 6259–6268. https://doi.org/10.1093/nar/gkp648.

Itoh, Y., Sekine, S., Yokoyama, S., 2012. Crystallization and preliminary X-ray crystallographic analysis of Aquifex aeolicus SelA, a bacterial selenocysteine synthase. Acta Crystallogr., Sect. F: Struct. Biol. Cryst. Commun. 68, 1128–1133. https://doi.org/10.1107/S1744309112033519.

Jumper, J., Evans, R., Pritzel, A., et al., 2021. Highly accurate protein structure prediction with AlphaFold. Nature 596, 583–589. https://doi.org/10.1038/s41586-021-03819-2.

Kaiser, J.T., Gromadski, K., Rother, M., Engelhardt, H., Rodnina, M.V., Wahl, M.C., 2005. Structural and functional investigation of a putative archaeal selenocysteine synthase. Biochemistry 44, 13315–13327. https://doi.org/10.1021/bi051110r.

Kinoshita, K., Nakamura, H., 2004. eF-site and PDBjViewer: database and viewer for protein functional sites. Bioinformatics 20, 1329–1330. https://doi.org/10.1093/bioinformatics/bth073.

Liebschner, D., Afonine, P.V., Baker, M.L., Bunkóczi, G., Chen, V.B., Croll, T.I., Hintze, B., Hung, L.-W., Jain, S., McCoy, A.J., Moriarty, N.W., Oeffner, R.D., Poon, B.K., Prisant, M.G., Read, R.J., Richardson, J.S., Richardson, D.C., Sammito, M.D., Sobolev, O.V., Stockwell, D.H., Terwilliger, T.C., Urzhumtsev, A.G., Videau, L.L., Williams, C.J., Adams, P.D., 2019. Macromolecular structure determination using X-rays, neutrons and electrons: recent developments in Phenix. Acta Crystallogr. D 75, 861–877. https://doi.org/10.1107/S2059798319011471.

Manzine, L.R., Cassago, A., da Silva, M.T.A., Thiemann, O.H., 2013a. An efficient protocol for the production of tRNA-free recombinant Selenocysteine Synthase (SELA) from Escherichia coli and its biophysical characterization. Protein Expr. Purif. 88, 80–84. https://doi.org/10.1016/j.pep.2012.12.005.

Manzine, L.R., Serrão, V.H.B., da Rocha e Lima, L.M.T., de Souza, M.M., Bettini, J., Portugal, R.V., van Heel, M., Thiemann, O.H., 2013b. Assembly stoichiometry of bacterial selenocysteine synthase and SelC (tRNAsec). FEBS Lett. 587, 906–911. https://doi.org/10.1016/j.febslet.2013.02.014.

Meng, E.C., Goddard, T.D., Pettersen, E.F., Couch, G.S., Pearson, Z.J., Morris, J.H., Ferrin, T.E., 2023. UCSF ChimeraX: tools for structure building and analysis. Protein Sci. 32, e4792 https://doi.org/10.1002/pro.4792.

Noinaj, N., Wattanasak, R., Lee, D.-Y., Wally, J.L., Piszczek, G., Chock, P.B., Stadtman, T. C., Buchanan, S.K., 2012. Structural insights into the catalytic mechanism of Escherichia coli selenophosphate synthetase. J. Bacteriol. 194, 499–508. https://doi.org/10.1128/jb.06012-11.

Palioura, S., Sherrer, R.L., Steitz, T.A., Söll, D., Simonovic, M., 2009. The human SepSecS-tRNASec complex reveals the mechanism of selenocysteine formation. Science 325, 321–325. https://doi.org/10.1126/science.1173755.

Paxman, J.J., Heras, B., 2017. Bioinformatics tools and resources for analyzing protein structures. Methods Mol. Biol. 16 (1549), 209–220. https://doi.org/10.1007/978-1-4939-6740-7_16.

Punjani, A., Rubinstein, J.L., Fleet, D.J., Brubaker, M.A., 2017. cryoSPARC: algorithms for rapid unsupervised cryo-EM structure determination. Nat. Methods 14, 290–296. https://doi.org/10.1038/nmeth.4169.

Ramírez-Aportela, E., Maluenda, D., Fonseca, Y.C., Conesa, P., Marabini, R., Heymann, J. B., Carazo, J.M., Sorzano, C.O.S., 2021. FSC-Q: a CryoEM map-to-atomic model quality validation based on the local Fourier shell correlation. Nat. Commun. 12, 42. https://doi.org/10.1038/s41467-020-20295-w.

Rayman, M.P., 2000. The importance of selenium to human health. Lancet 356, 233–241. https://doi.org/10.1016/S0140-6736(00)02490-9.

Schimmel, P.R., Söll, D., 1979. Aminoacyl-tRNA synthetases: general features and recognition of transfer RNAs. Annu. Rev. Biochem. 48, 601–648. https://doi.org/10.1146/annurev.bi.48.070179.003125.

Schön, A., Böck, A., Ott, G., Sprinzl, M., Söll, D., 1989. The selenocysteine-inserting opal suppressor serine tRNA from E. coli is highly unusual in structure and modification. Nucleic Acids Res. 17, 7159–7165. https://doi.org/10.1093/nar/17.18.7159.

Serrão, V.H.B., Regina Manzine, L., e Silva, I.R., Cassago, A., Bettini, J., Villares Portugal, R., van Heel, M., Henrique Thiemann, O., 2014. Investigation of Escherichia coli selenocysteine synthase (SelA) complex formation using cryo-electron microscopy (Cryo-EM). Microsc. Microanal. 20, 1282–1283. https://doi.org/10.1017/S1431927614008149.

Serrão, V.H.B., Scortecci, J.F., 2020. Why selenocysteine is unique? Front. Mol. Biosci. 7 https://doi.org/10.3389/fmolb.2020.00002.

Serrão, V.H.B., Silva, I.R., da Silva, M.T.A., Scortecci, J.F., de Freitas Fernandes, A., Thiemann, O.H., 2018. The unique tRNASec and its role in selenocysteine biosynthesis. Amino Acids 50, 1145–1167. https://doi.org/10.1007/s00726-018-2595-6.

Silva, I.R., Serrão, V.H.B., Manzine, L.R., Faim, L.M., da Silva, M.T.A., Makki, R., Saidemberg, D.M., Cornélio, M.L., Palma, M.S., Thiemann, O.H., 2015. Formation of a ternary complex for selenocysteine biosynthesis in bacteria. J. Biol. Chem. 290, 29178–29188. https://doi.org/10.1074/jbc.M114.613406.

Stadtman, T.C., 1996. Selenocysteine. Annu. Rev. Biochem. 65, 83–100. https://doi.org/10.1146/annurev.bi.65.070196.000503.

Stadtman, T.C., 1974. Selenium biochemistry. Science 183, 915–922. https://doi.org/10.1126/science.183.4128.915.